LS3D and 2LCMFlow benchmark results

Saeedeh Yavari-Ramshe[a] and Behzad Ataie-Ashtiani[a]

[a]Sharif University of Technology, Civil Engineering Department, Tehran, Iran

This paper describes the simulation results of LS3D [1] and 2LCMFlow [8] models for five benchmark problems and a case study provided in the 2017 NTHMP Benchmark Workshop. The LS3D model is a finite difference implementation of the 4th order Boussinesq equations, considering landslide as a time variable bottom boundary with a rigid hyperbolic-shaped geometry. This model is applied for the simulation of the tsunami waves caused by a solid landslide in benchmarks 2 and 3. The 2LCMFlow model is a finite volume solution of the incompressible Euler equations for a two-layer two-phase flow model. In this model, landslide is described as a layer of a two-phase Coulomb mixture moving beneath a layer of water. This model is applied to study benchmarks 4 and 5 where landslide is deformable. Both models are able to predict the landslide-generated waves (LGWs) with a computational error less than 10%. LS3D is more accurate in simulating the wave propagation stage while 2LCMFlow predicts the wave generation stage more accurately. 2LCMFlow also predicts landslide deformations properly. Finally, the LS3D is applied to simulate the 1964 landslide event of Port Valdez, Alaska. The predicted values of run-up heights, wave amplitudes, and the estimated flood areas are mostly overestimated although fairly close to the observed data. It is probably due to considering a rigid landslide in LS3D model. To achieve a better estimation for wave runup heights and flood affected areas, the combined effects of earthquake and both landslides should be considered using a more capable model.

1. Numerical models

1.1. LS3D model

LS3D is a two-dimensional depth-integrated numerical model based on a fourth-order Boussinesq type approximation [1]. This model was originally developed in 2007 by Ataie-Ashtiani and Najafi-Jilani to simulate submarine landslide-generated waves. In LS3D, landslide is described as a time-variable bottom boundary with a rigid hyperbolic-shaped geometry moving along the bed. The model was verified using the laboratory data of Enet et al. (2003) and Grilli et al. (2002) in a three-dimensional wave tank for a submerged rigid sliding block [2, 3]. LS3D has been applied to estimate the consequences of three potential landslide scenarios in Shafarood dam reservoir, north of Iran.

In 2011, the model was extended to simulate the impulsive waves caused by not only submarine landslides but also subaerial cases [4]. The extended model was verified based on 120

experimental tests of [5] on subaerial landslide-generated waves. Ataie-Ashtiani and Yavari-Ramshe (2011) applied the extended model to predict the probable runup heights and dam overtopping of potential subaerial landslides for Maku and Shafaroud dam reservoirs located in the northwestern and north parts of Iran, respectively [4, 6].

1.1.1. Model equations

The LS3D mathematical formulation is an extension of (4,4) Padé approximant for moving bottom boundary, based on a higher-order perturbation analysis using the expanded form of velocity components which results in the following fourth-order Boussinesq-type mass conservation and momentum equations [1]:

$$
\begin{aligned}
\frac{1}{\varepsilon}h_t + \zeta_t + \nabla.\Big\{ & (\varepsilon\zeta + h)\mathbf{u_0} \\
& + \mu^2\Big[\tfrac{-1}{6}(\varepsilon^3\zeta^3 + h^3)\mathbf{A} + \tfrac{1}{2}\tilde{z}^2(\varepsilon\zeta + h)\mathbf{A} - \tfrac{1}{2}(\varepsilon^2\zeta^2 - h^2)(\nabla.B) + \tilde{z}^2(\varepsilon\zeta + h)(\nabla.B)\Big] \\
& + \mu^4\Big[\tfrac{1}{120}(\varepsilon^5\zeta^5 + h^5)\nabla(\nabla.\mathbf{A}) - \tfrac{1}{24}(\varepsilon\zeta + h)\tilde{z}^4\nabla(\nabla.\mathbf{A}) - \tfrac{1}{12}(\varepsilon^3\zeta^3 + h^3)\nabla(\nabla.(\tilde{z}^2.\mathbf{A})) \\
& \quad + \tfrac{1}{4}(\varepsilon\zeta + h)\tilde{z}^2\nabla(\nabla.(\tilde{z}^2\mathbf{A})) + \tfrac{1}{24}(\varepsilon^4\zeta^4 - h^4)\nabla(\nabla.(\nabla B)) - \tfrac{1}{6}(\varepsilon\zeta + h)\tilde{z}^3\nabla(\nabla.(\nabla B)) \\
& \quad - \tfrac{1}{6}(\varepsilon^3\zeta^3 + h^3)\nabla(\nabla.(\tilde{z}\nabla B)) + \tfrac{1}{2}(\varepsilon\zeta + h)\tilde{z}\nabla(\nabla.(\tilde{z}\nabla B)) \\
& \quad + \tfrac{1}{2}(\varepsilon^2\zeta^2 - h^2)\nabla C - (\varepsilon\zeta + h)\tilde{z}\nabla C\Big] \Big\} = O(\varepsilon^6, \mu^6)
\end{aligned}
$$

(1)

$$
\begin{aligned}
\mathbf{u_{0t}} + \varepsilon(\nabla.\mathbf{u_0})\mathbf{u_0} & + \varepsilon\big(w_1\big|_{z=0}\big)\mathbf{u_{0z}} \\
& + \mu^2\Big[\mathbf{u_{1t}}\big|_{z=0} + \varepsilon(\nabla.(\mathbf{u_1}\big|_{z=0}))\mathbf{u_0} + \varepsilon(\nabla.\mathbf{u_0})(\mathbf{u_1}\big|_{z=0}) + \varepsilon\big(w_2\big|_{z=0}\big)\mathbf{u_{0z}} + \big(w_1\big|_{z=0}\big)\big(\mathbf{u_{1z}}\big|_{z=0}\big)\Big] \\
& + \mu^4\Big[\mathbf{u_{2t}}\big|_{z=0} + \varepsilon(\nabla(\mathbf{u_2}\big|_{z=0}))\mathbf{u_0} + \varepsilon(\nabla.(\mathbf{u_1}\big|_{z=0}))(\mathbf{u_1}\big|_{z=0}) + \varepsilon(\nabla.\mathbf{u_0})(\mathbf{u_2}\big|_{z=0}) \\
& \quad + \varepsilon\big(w_2\big|_{z=0}\big)\big(\mathbf{u_{1z}}\big|_{z=0}\big) + \big(w_1\big|_{z=0}\big)\big(\mathbf{u_{2z}}\big|_{z=0}\big)\Big] \\
& + \nabla\big(P\big|_{z=0}\big) = O(\varepsilon^6, \mu^6)
\end{aligned}
$$

(2)

Eq. 1 and Eq. 2 represent the continuity and the depth-averaged momentum equations in the two horizontal x and y directions, respectively. $\varepsilon = \frac{a_0}{h_0}$ and $\mu = \frac{h_0}{L_0}$ are two indexes indicating wave nonlinearity and dispersive behaviour. a_0, L_0, and h_0 respectively stand for a characteristic wave amplitude, wave length and water depth. The subscripts represent the partial derivative (e.g. $h_t = \frac{\partial h}{\partial t}$). t is time, h water depth, ζ the water surface fluctuations, p the water pressure, and $\nabla = (\frac{\partial}{\partial x}, \frac{\partial}{\partial y})$ the horizontal gradient vector. $\mathbf{u} = (u, v)$ and w represent the vector of the horizontal velocity components and the vertical velocity component in the z direction, respectively. The velocity domain components are expanded into [1]

$$\mathbf{u} = \mathbf{u_0} + \mu^2.\mathbf{u_1} + \mu^4.\mathbf{u_2} \tag{3}$$

$$w = \mu^2.w_1 + \mu^4.w_2 \tag{4}$$

in perturbation analysis with μ^2 as the basic small parameter. $\tilde{z}$ is a characteristic variable depth defined as a weighted average of two distinct water depths z_a and z_b based on $\tilde{z} = [\beta. z_a + (1 - \beta). z_b]$. β is an optimized weighting parameter. Moreover, $\mathbf{A} = \nabla(\nabla. \mathbf{u}_0)$, $\mathrm{B} = \nabla. (h\mathbf{u}_0) + \frac{1}{\varepsilon} h_t$, and $\mathrm{C} = f(\mathbf{A}, \mathrm{B})$. A schematic definition of the model parameters can be observed in Fig. 1.
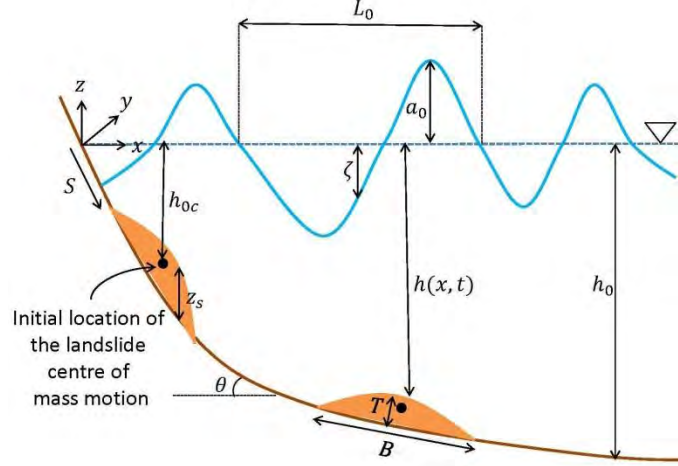

Fig. 1 The LS3D model parameters and assumptions

As it was mentioned above, LS3D describes landslide as a time variable bottom boundary with a rigid hyperbolic-shape geometry. The law of the mass motion is [3]

$$S(t) = S_0 \ln(\cosh\frac{t}{t_0}) \tag{5}$$

Where S is the location of landslide centre of mass motion parallel to the slope, $S_0 = u_t^2/a_0$, and $t_0 = u_t/a_0$. u_t is the terminal velocity of the sliding mass and a_0 is its initial acceleration defined as [3]

$$u_t = \sqrt{gB}. \sqrt{\frac{\pi(\gamma-1)}{2C_d}}. \sin\theta \quad , \quad a_0 = g\frac{\gamma-1}{\gamma+C_m}\sin\theta \tag{6}$$

where $\gamma = \rho_S/\rho_w$, B is the length of the sliding mass along the inclined bed, C_d is the drag coefficient, C_m is the added mass coefficient, θ is the bed slope and g is the gravitational acceleration. ρ_s and ρ_w are the landslide and the water densities, respectively. The mass motion equation is obtained by transforming Eq. 5 from the bottom direction to the Cartesian coordinate (x, y, z) direction. Accordingly, the time variable bottom boundary is obtained as [4]

$$h(x,t) = h_0(x) - 0.5T\left(1 + \tanh\left(\frac{x-x_l(t)}{\acute{S}}\right)\right)\left(1 - \tanh\left(\frac{x-x_r(t)}{\acute{S}}\right)\right) \tag{7}$$

where $x_l(t) = x_c(t) - 0.5T\cos\theta$ and $x_r(t) = x_c(t) + 0.5T\cos\theta$ are the locations of the rear and the front ends of the sliding mass, respectively. $x_c(t)$ is the location of the sliding mass

centre, T is the maximum mass thickness and $\acute{S} = o.5/cos\theta$. Eq. 7 determines the location of the sliding mass center at each time step.

For the three-dimensional conditions, a truncated hyperbolic secant function of x and y with a specific truncation ratio, r, as introduced by [2], is applied to describe the landslide model geometry.

$$\begin{cases} z_s(x,y) = \frac{T}{r}(sech(K_w x).sech(K_B y) - (1-r)) & z_s \geq 0 \\ K_w = \frac{2}{w}\text{asech}\left(\frac{1-r}{r}\right), & K_B = \frac{2}{B}\text{asech}\left(\frac{1-r}{r}\right) \end{cases} \tag{8}$$

where z_s is the thickness of the sliding mass moving along the bed. The specific truncation ratio can be modified according to the real geometry of the sliding mass. The effects of the solid block movements on the water surface fluctuations is inserted into the model equations through the kinematic boundary condition of the bed which is [4]

$$h_t + \mathbf{u}.\nabla h = -w \quad z = -h \tag{9}$$

The original LS3D was able to model submarine landslides [1]. In 2011, the model was extended to handle subaerial landslide cases [4] based on the method of [7]. According to Eqs. 4 and 5, the kinematic characteristics of the sliding mass depend on u_t, and a_0. For subaerial cases, landslide velocity must be altered to include the effects of the aerial acceleration. Accordingly, they formulated the sliding velocity as a weighted average of the aerial and submerged velocities, where the weighting parameter is based on the fraction of the submerged volume. The slope-parallel velocity of the slide is calculated as [7]

$$f_s u_s + f_a gtsin\theta \tag{10}$$

The coefficients f_s and f_a represent the submerged and the aerial volume fractions of the landslide, respectively. The time-dependent velocity of a submerged landslide, u_s, is calculated as [3]

$$u_s = u_t \text{tanh}(\frac{t}{t_0}) \tag{11}$$

This linear combination of the aerial and submerged velocities is used instead of terminal velocity, u_t, in Eq. 6 [4].

The model inputs include the domain topography, the water surface level, h_0, reflection factor, F (representing the reflection percentage of the lake borders), the geometrical properties of the landslide including the sliding mass length, B, width, w, and maximum thickness, T, the relative density γ, the slide initial depth, h_{0c}, the sliding slope angle, θ, the drag coefficient, C_d, and the added mass coefficient, C_m.

1.1.2. Numerical method

In LS3D, a sixth-order multi-step finite difference method is applied for spatial discretization and a sixth-order Runge–Kutta method is implemented for temporal discretization of the higher-order depth-integrated governing equations and boundary conditions. The details are given in [1].

1.2. 2LCMFlow model:

2LCMFlow is a two-layer two-phase shallow water type model developed by [8] based on the incompressible Euler equations. The model includes a layer of granular material moving beneath a layer of water. The sliding mass is described as a Coulomb mixture; a two-phase mixture of water and solid grains where its interaction with the bottom follows a Coulomb-type friction law and the normal and longitudinal stresses of the solid phase are related with the earth pressure coefficient, K. The definition of the constitutive structure of landslide makes the model able to simulate a variety of the sliding masses having dense to loose material. The model is able to capture the simultaneous appearance of flowing/static region along the landslide runout path by considering a critical basal stress based on the angle of repose of the sliding material.

2LCMFLow model is validated against two sets of experimental data on both submarine [9, 10] and subaerial [5] landslide-generated waves. The model is now applying to study the effects of landslide rheological, geotechnical, and constitutive properties on both landslide deformations and LGWs characteristics [11].

1.2.1. Model equations

The final system of model equations for this two-layer Coulomb mixture flow (2LCMFlow) model can be written as [8]

$$\begin{cases} h_{1t} + (q_1 cos\theta)_x = 0 \\ q_{1t} + \left(h_1 u_1^2 cos\theta + g\frac{h_1^2}{2}cos^3\theta\right)_x = -gh_1 cos\theta b_x + g\theta_x \frac{h_1^2}{2}sin\theta cos^2\theta \\ \quad -gh_1 cos\theta (h_2 cos^2\theta)_x \\ h_{2t} + (q_2 cos\theta)_x = 0 \\ q_{2t} + \left(h_2 u_2^2 cos\theta + g\Lambda_2 \frac{h_2^2}{2}cos^3\theta\right)_x = -gh_2 cos\theta b_x + g\theta_x \frac{h_2^2}{2}sin\theta cos^2\theta \\ \quad -rgh_2\Lambda_1 cos\theta (h_1 cos^2\theta)_x + \frac{\Im}{cos\theta} \end{cases} \qquad (12)$$

Subscript 1 and 2 represent the water and the granular layers, respectively. θ is the local bed slope and $b(x)$ is the bottom topography. Moreover, $q = hu$, , $\Lambda_1 = \lambda_1 + K(1 - \lambda_1)$, and

$\Lambda_2 = r\lambda_2 + K(1 - r\lambda_2).$ $K = 2\left(1 - sgn(u_{2x})\sqrt{1 - \left(\frac{cos\phi}{cos\delta_{mod}}\right)^2}\right)/cos^2\phi - 1$ is the earth

pressure coefficient and $tan\delta_{mod} = tan\delta - \lambda'Kh_{2x}$. $r = \rho_2/\rho_1$ represents landslide relative density. ρ_1 and ρ_2 show water and landslide densities, respectively. Parameters ϕ and δ stand for the internal and the basal friction angles of the granular layer, respectively. δ_{mod} shows a dynamic modification of the basal friction angle and λ' is a constant. Finally, $\Im$ stands for the Coulomb friction term defined as [8]

$$\begin{cases} \Im = -(g(1-r)h_2cos^2\theta + h_2u_2^2cos\theta(sin\theta)_x)\frac{q_2}{|q_2|}tan\delta_{mod} & |\Im| \geq \sigma_c \\ q_2 = 0 & |\Im| < \sigma_c \end{cases} \tag{13}$$

where σ_c is a basal critical stress which is defined based on δ_0, the angle of repose of the granular material, as $\sigma_c = g(1-r)h_2cos\theta tan\delta_0$. Based on Eq. 13, landslide stops moving wherever its angle is less than the angle of repose. The constitutive structure of the sliding material is defined using two coefficients λ_1 and λ_2 which distribute the water layer pressure between the solid and the fluid phases of the second layer on the interface and along the second layer, respectively [8]

$$\begin{cases} P^f_{2zz} = \lambda_1\rho_1h_1cos\theta + \lambda_2\rho_1(h_2 - z)cos\theta \\ P^s_{2zz} = (1 - \lambda_1)\rho_1h_1cos\theta + (\rho_2 - \lambda_2\rho_1)(h_2 - z)cos\theta \end{cases} \tag{14}$$

In Eq. 14, P_{zz} is the normal stress and the superscripts f and s stand for the fluid and the solid phases of the second layer (the sliding mass), respectively. A schematic of the model parameters is illustrated in Fig. 2.
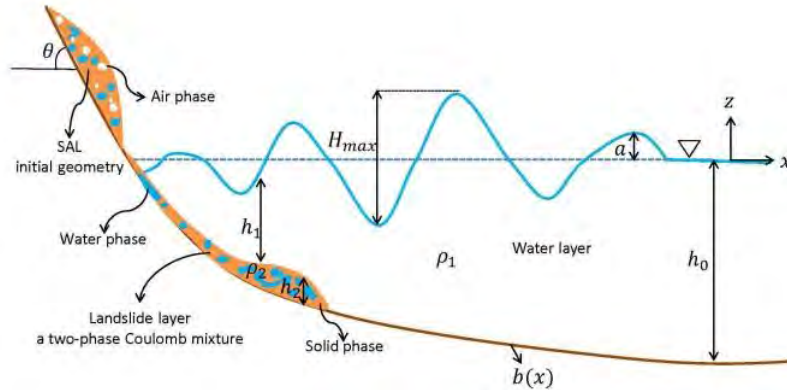

Fig. 2 Schematic definition of the 2LCMFlow model parameters and assumptions

1.2.2. Numerical method

To discretize the system of model equations for 2LCMFlow, a well-balanced second-order Roe-type finite volume method is applied which is introduced by [12] as a state of the art of

6

numerical methods. This scheme is a two-step Roe-type finite volume upwinding the source terms [12]. The non-homogeneous terms regarding the bed level and the bed curvature are upwinded in the same way of the numerical fluxes while the Coulomb friction term is discretized using a two-step semi-implicit approach.

Regarding the wet/dry borders, a modified wet/dry treatment based on the non-linear method of [13] is applied in 2LCMFlow which makes the model able to deal with various situations of wet/dry transitions. This method is modified to deal with not only the bed level but also the bed curvature changes [12].

2. Benchmark problem comparisons

2.1. Benchmark problem #2: Three-dimensional submarine solid block

In these experiments, landslide is a rigid Gaussian-shaped body. The LS3D model parameters are supposed to be $\Delta x = \Delta y = 0.1\ m$, and $\Delta t = 0.1\ s$. The numerical results are compared with the experimental data for seven different values of initial landslide submergence depth, d, in Fig. 3. The wave generation and propagation patterns are in a good agreement. The root mean square error (RMSE) for the first five seconds of wave propagation is calculated in Table 1 for different values of landslide initial submergence depth. RMSEs are calculated without the effects of time phase differences. For this benchmark problem, RMSEs are up to 3.93 with an average value of 1.42 which demonstrates the proper accuracy of LS3D in predicting the impulsive waves caused by rigid landslides.

Table 1 RMSEs in Gauges 1-4 for the first 5 *sec* of wave propagation; Benchmark #2

Gauge no.	d (*mm*)						
	61	80	100	120	140	149	189
g1	1.19	1.39	1.03	0.77	0.53	0.53	0.34
g2	2.38	2.53	1.72	1.09	0.82	0.52	0.34
g3	2.71	3.93	-	-	2.04	-	1.06
g4	2.23	2.70	2.00	1.23	0.99	0.64	0.53

Fig. 4 compares the numerical and experimental values of maximum LGW height, $H_{max} = \eta_{max} + \eta_{min}$ and shows an average relative error of about 7.5%. η_{max} and η_{min} represents the maximum positive and negative wave amplitudes, respectively. As it can be observed in Fig. 3, numerical waves dissipate faster than experimental LGWs. This is probably due to the numerical dispersion of LS3D model equations which also creates a time phase difference of about 10-15%. This time differences make the numerical LGWs move slower than the experimental LGWs. As a result, these Boussinesq-type wave equations (BWEs) generally overestimate the wave dispersion which results in underestimating the maximum wave heights close to the

shorelines. Moreover, wave runup heights may also be underestimated. However, BWEs estimate the nonlinearity and dispersive behavior of the generated waves much better than the shallow water type equations and provide a powerful tool for predicting the near-field and far-field characteristics of LGWs [14].
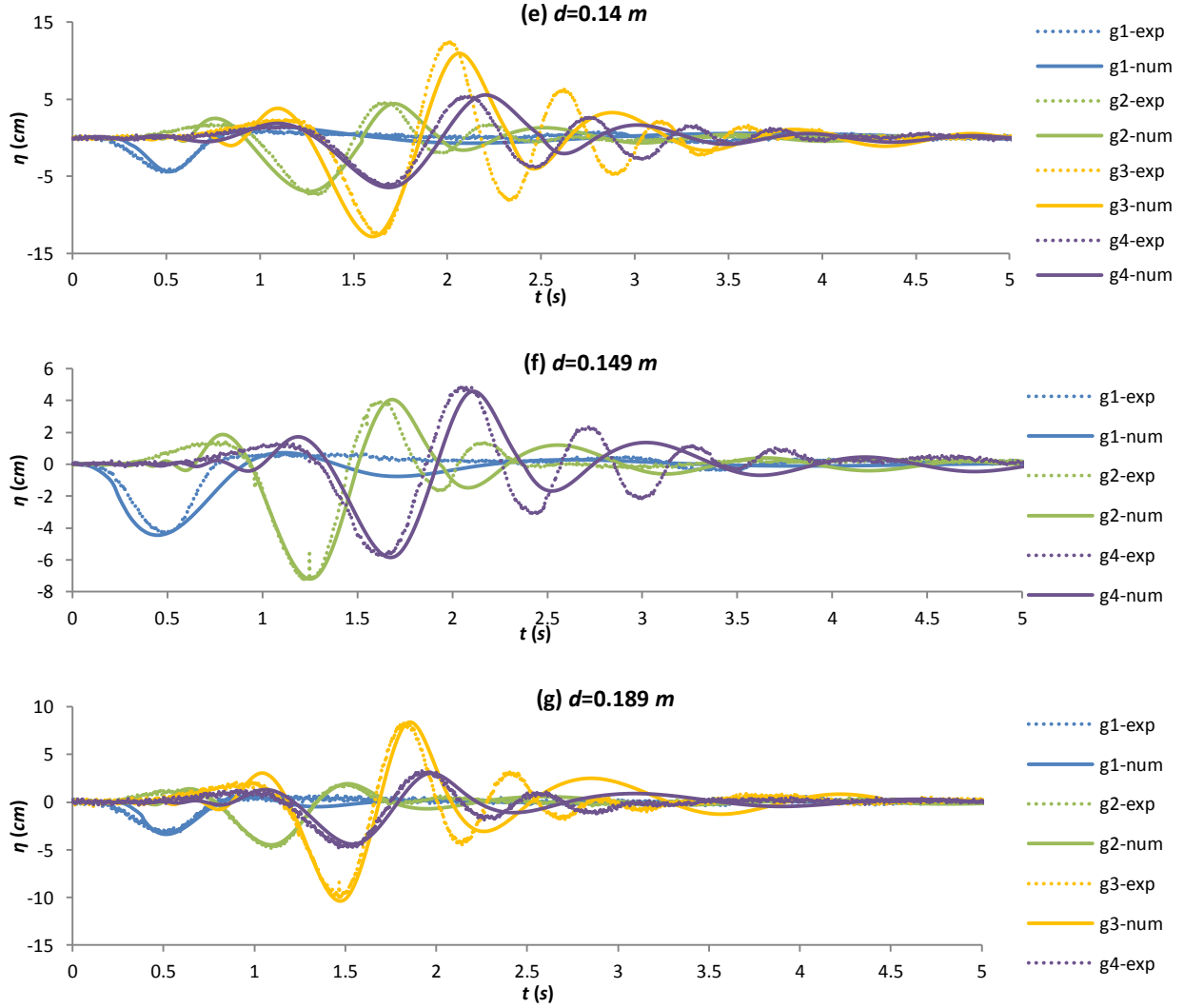
8
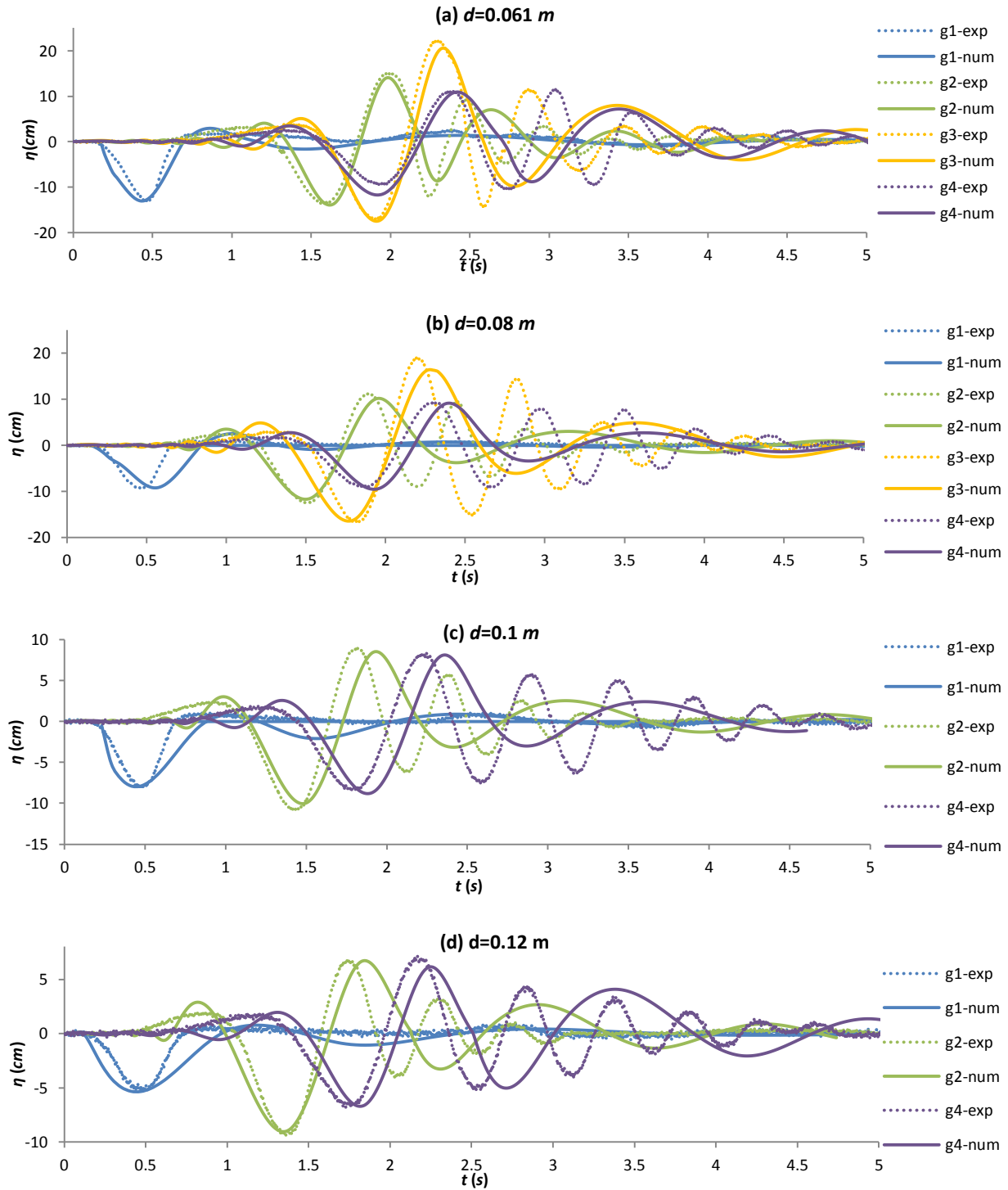
Fig. 3 Comparison between LS3D results and experimental data of temporal water surface fluctuations in four different gages (g1-g4) for seven different initial landslide submergence depths, *d*. benchmark problem #2

Finally, the runup values are estimated based on the empirical equation introduced by [14] as

$$\frac{R_u}{h_0} = 2.831 \left(\frac{H}{h_0}\right)^{1.25} \sqrt{cot\beta} \qquad (15)$$

using the wave heights, H, predicted by LS3D close to the runup area. In this equation, R_u represents the runup height and β is the slope angle of the runup surface. These runup values are compared with the experimental measurements of [15] in Fig. 5. The relative errors are up to 26% with an average value of about 15%. Based on Fig. 5, the runup values are generally underestimated by LS3D which may be caused by numerical dispersion.
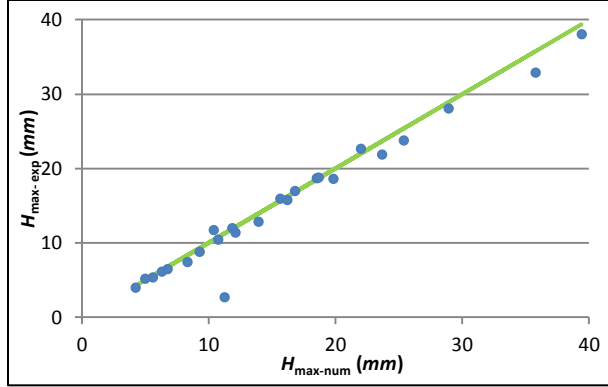
Fig. 4 Comparison between the numerical and experimental values of the maximum wave heights for benchmark problem #2
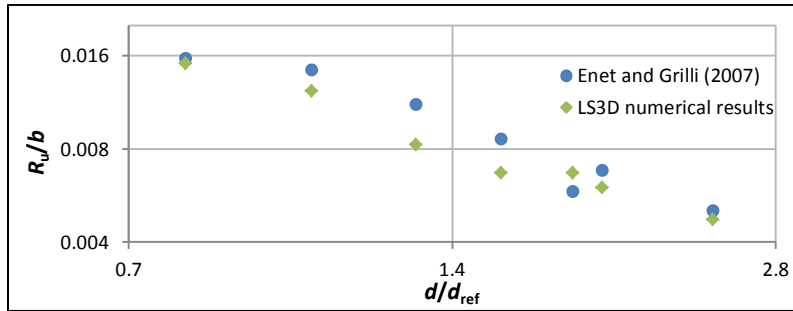

Fig 5 Runup values for Benchmark #2; Comparison between numerical results of LS3D and experimental measurements

2.2. Benchmark problem #3: Three-dimensional submarine/subaerial solid block

The LS3D model parameters are $\Delta x = \Delta y = 0.1\ m$, and $\Delta t = 0.1\ s$. The numerical results are compared with the experimental data in Fig. 6 and Fig. 7 for submarine landslide (SML) and subaerial landslide (SAL) cases, respectively. Again, there is a good agreement between the numerical and experimental data. Table 2 includes the relative errors, Er, calculated for the maximum positive, a_{pmax}, and negative, a_{nmax}, wave heights of the first generated waves. The relative errors show that the wave amplitudes are between 5%-15% overestimated by the LS3D model. A part of these errors is due to landslide geometry. LS3D considers a hyperbolic-shaped geometry for the landslide while in these experiments the sliding block has a wedge-shaped geometry. The wave amplitudes are more overestimated for SAL case rather than the SML case. This discrepancy is most likely because of the considered modifications in LS3D for simulating the SAL cases. A linear combination of the landslide plunging velocity and its underwater terminal velocity is applied as the kinematic condition of the sliding block. Accordingly, the wave generation mechanism by a SAL is considered to be the same as the wave generation mechanism by a SML.
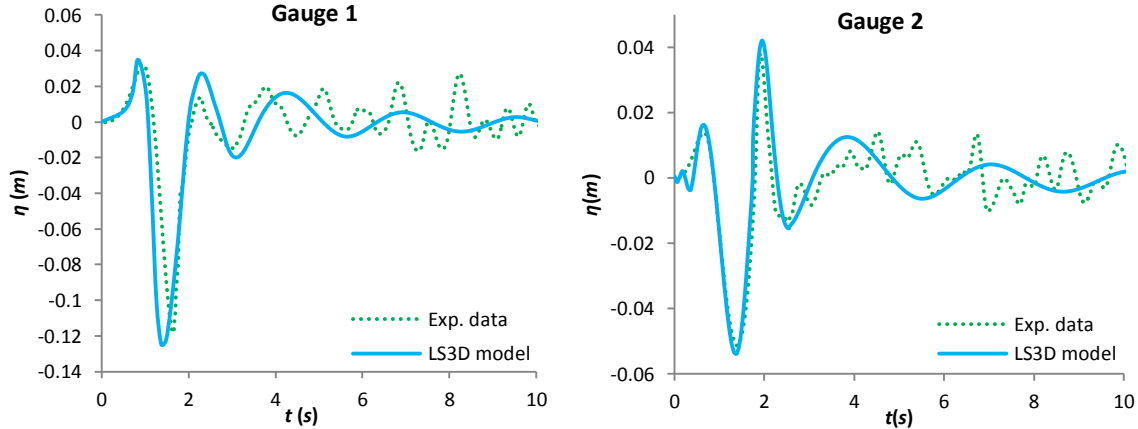
10

Fig. 6 Water surface fluctuations for SML case of benchmark #3; Comparison between the LS3D model results and experimental data
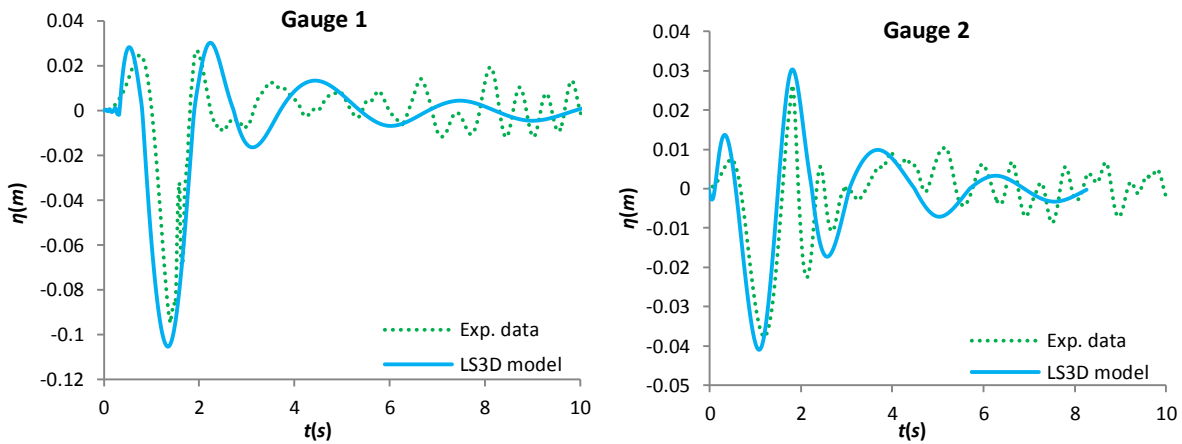

Fig. 7 Water surface fluctuations for SAL case of benchmark #3; Comparison between the LS3D model results and experimental data

Table 2 The relative error and RMSEs calculated regarding the wave amplitudes in benchmark #3

Test no.	Gauge no.	Wave amplitude (m)			Er (%)	RMSE (%)
		symbole	Exp.	Num.		
SML	1	a_{pmax}	0.0346	0.0322	7.37	1.78
		a_{nmax}	-0.1246	-0.1183	5.32	
	2	a_{pmax}	0.0421	0.0382	10.3	0.70
		a_{nmax}	-0.0538	-0.0512	5.05	
SAL	1	a_{pmax}	0.0266	0.0303	14.07	0.72
		a_{nmax}	-0.0948	-0.1052	10.98	
	2	a_{pmax}	0.0264	0.0302	14.67	0.86
		a_{nmax}	-0.0377	-0.0409	8.72	

2.3. Benchmark problem #4: Two-dimensional submarine granular slide

In these experiments, the sliding mass is a series of triangular cavities filled with glass beads with a diameter of $d_b = 4\ mm$. Test 17 is the one which is simulated using 2LCMFlow model. The slide porosity is supposed to be ψ_0=36.6% which leads to a bulk density of about $\rho_b = 1951\ kg/m^3$ with a relative density of $\gamma = 1.951$ [16]. The internal and basal friction angles are also considered to be $\phi = 34°$ and $\delta = 24°$, respectively [16]. The angle of repose is $\delta_0 = 25°$. The constitutive parameters of λ_1 and λ_2 are calibrated as 0.1 and 0.25 to achieve the best fit regarding both landslide deformations and water surface fluctuations. The model parameters are $\Delta x = 0.01\ m$, and $\Delta t = 0.005\ s$. The 2LCMFlow numerical results are compared with the experimental data in Fig. 8.
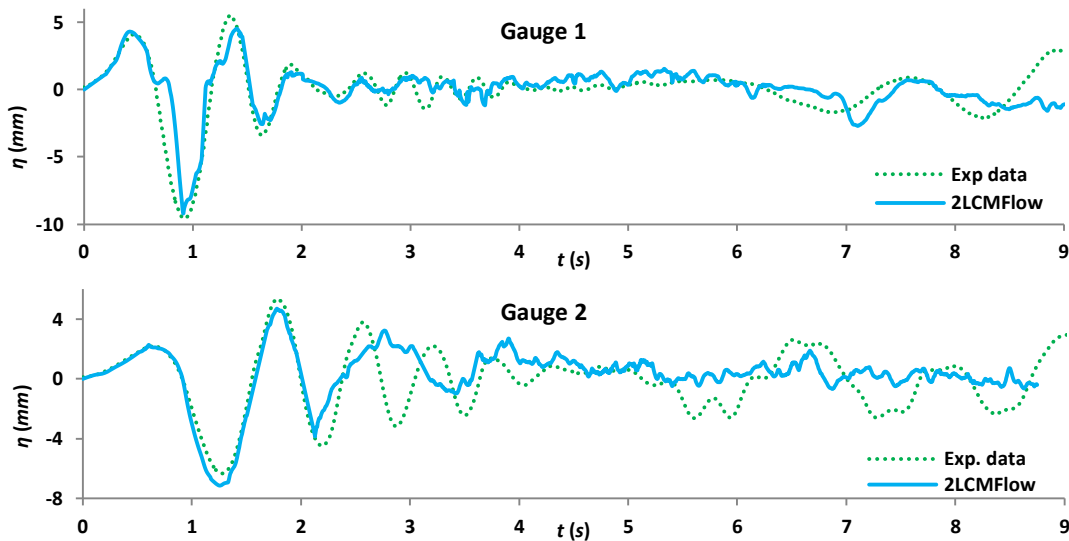

Fig. 7 Water surface fluctuations in gauge 1 and 2 for benchmark #4; Comparison between experimental data and numerical results of the 2LCMFlow model

2LCMFlow is able to simulate the wave generation stage more accurately in comparison with LS3D that generally overestimates the first generated wave. However, as it can be observed in Fig. 7, the numerical waves are dissipated faster than the experimental waves. Accordingly, the model is not able to predict the wave propagation at gauges 3 and 4 properly. This is because of the intrinsic limitation of the Shallow Water Equations (SWEs) in simulating the wave dispersion which can be solved by applying the Boussinesq-type models with higher order of wave dispersion and nonlinearity such as LS3D for the wave propagation stage. Non-hydrostatic corrections are another alternative to improve the ability of depth-averaged type equations for simulating wave nonlinear and dispersive behavior [17]. The RMSEs are calculated as 1.27 and 2.76 for the first and the second gauges, respectively. The wave amplitudes are estimated with a relative error of up to 15%. The time difference between the numerical and the experimental waves is less than 5% for 2LCMFlow.

Fig. 8 shows the depth profiles of the sliding mass in various times in comparison with the photos taken during the slide motion in experiment 17. Both landslide deformations and water surface fluctuations obey their equivalent experimental patterns. This fact demonstrates the ability of 2LCMFlow in simulating the simultaneous interactions of landslide and water.
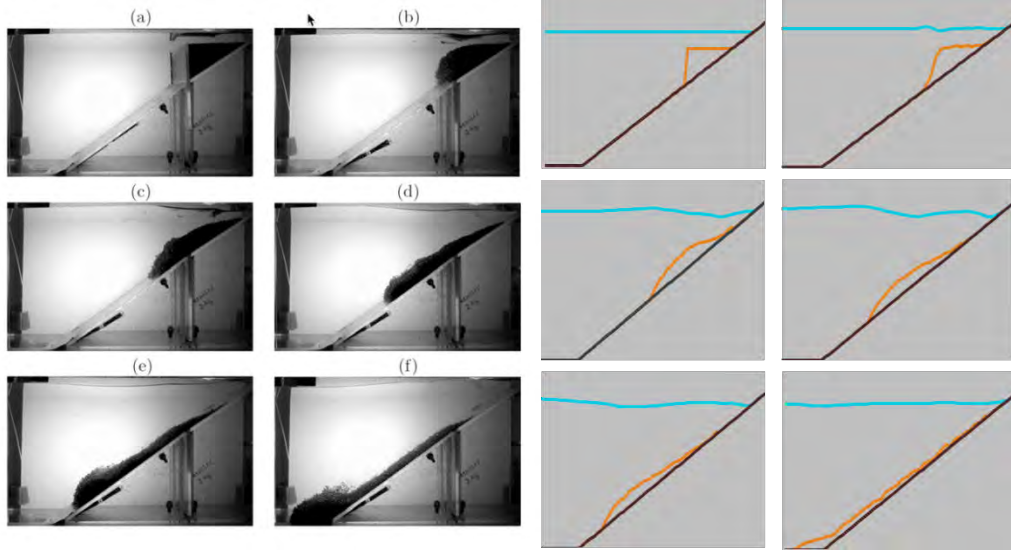

Fig. 8 Visual comparison of landslide depth profiles at times (a) 0.0, (b) 0.02, (c) 0.17, (d) 0.32, (c) 0.47, and (f) 0.62 seconds for benchmark #4, experiment 17.

2.4. Benchmark problem #5: Two-dimensional subaerial granular slide

In these experiments, landslide is a wedge-shaped cavity filled with glass beads having a dry density of $\rho_s = 2500 \, kg/m^3$. Table 3 shows the 2LCMFlow model parameters which are considered for the two simulated experiments. In these simulations, $\Delta x = 0.01 \, m$, and $\Delta t = 0.001 \, s$. The numerical results for water surface fluctuations are compared with the experimental data in figures 9 and 10 for case 1 and case 2, respectively. The numerical and experimental waves are in a good agreement with RMSE between 0.2-0.5 for the first 2.5 sec. The average relative error of wave amplitudes is about 8%.

Table 3 2LCMFlow Model parameters for benchmark #5

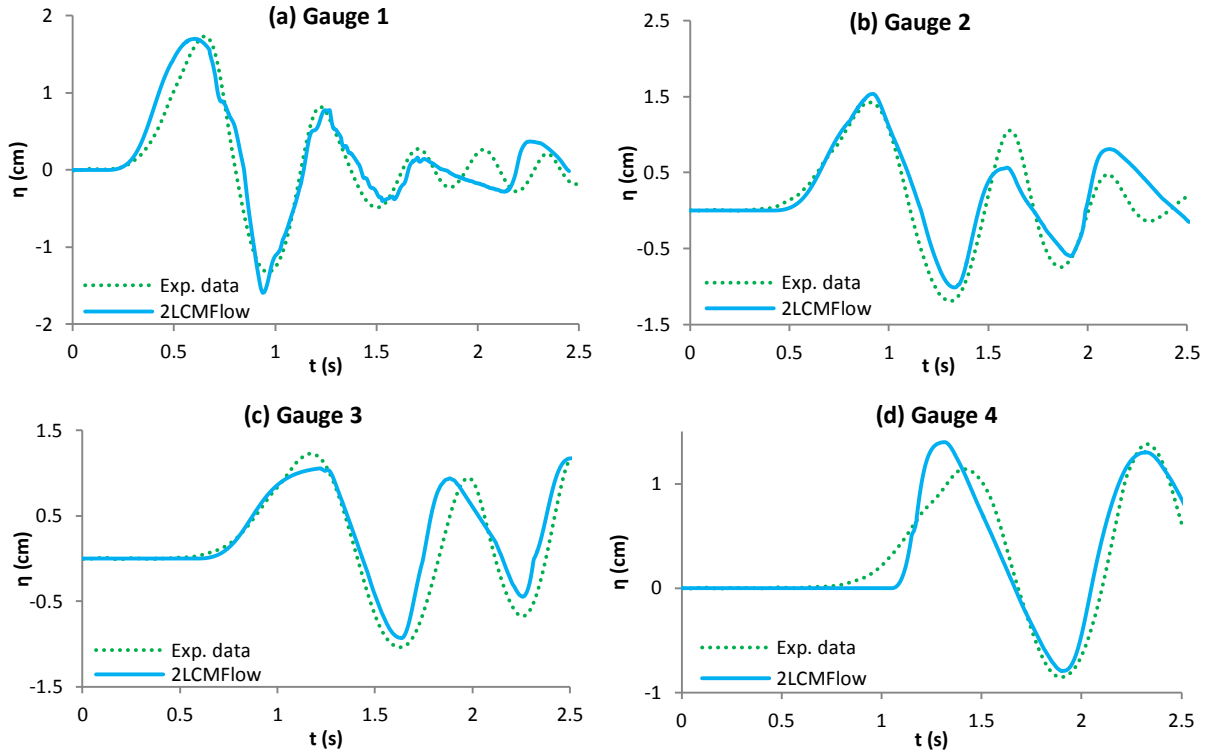| Parameter		Case 1	Case 2
Landslide bulk density	ρ_b	$1900 \, kg/m^3$	$1750 \, kg/m^3$
Internal friction angle	ϕ	34°	25°
Basal friction angle	δ	10°	15°
Angle of repose	δ_0	25°	20°
Landslide porosity	ψ_0	0.4	0.5
Constitutive parameter	λ_1	0.75	0.4
Constitutive parameter	λ_2	0.25	0.5

Fig 9 Water surface fluctuations at gauges 1-4 for case 1 of benchmark #5; Comparison between 2LCMflow numerical results and experimental measurements
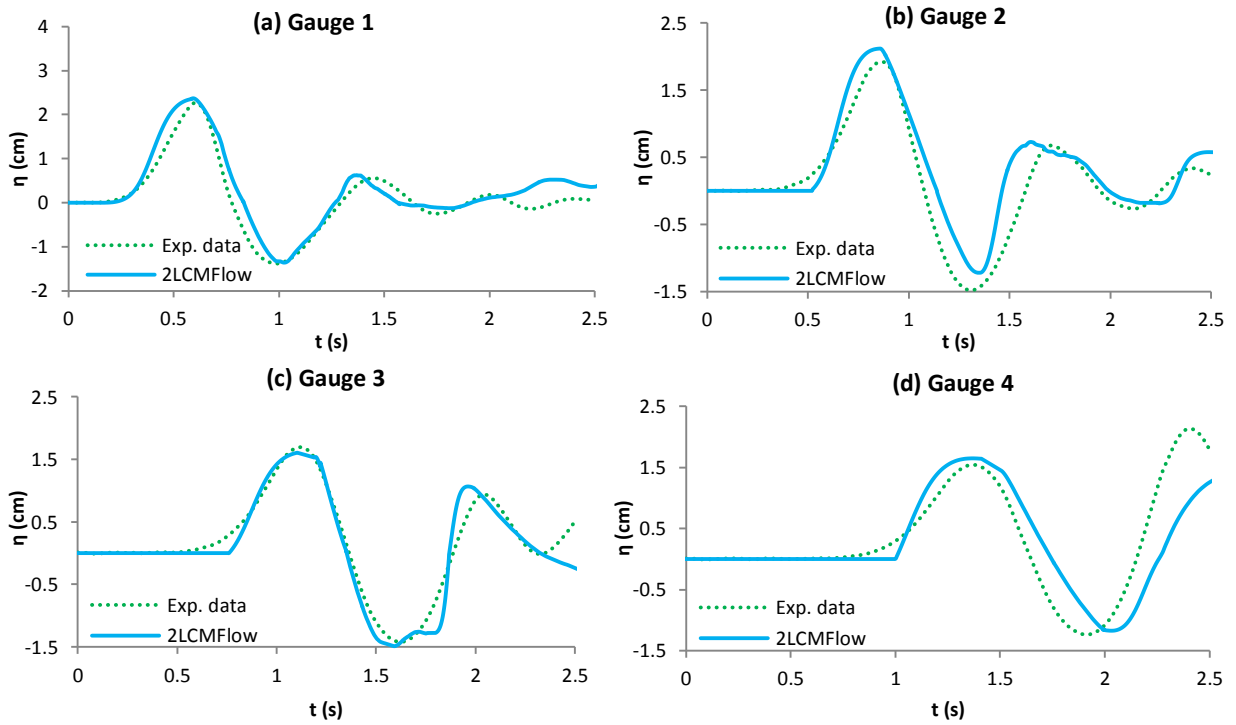

Fig 10 Water surface fluctuations at gauges 1-4 for case 2 of benchmark #5; Comparison between 2LCMflow numerical results and experimental measurements

In Fig 11, landslide deformation profiles predicted by 2LCMFlow are visually compared with the experimental photos of case 1 [18] at different times. Both landslide deformations and water surface fluctuations are in good agreement between the numerical and the experimental results. Unfortunately, there is no recorded data on landslide deformations in these experiments. However, based on the available photo, the computational errors regarding landslide deformations are approximately less than 10%.
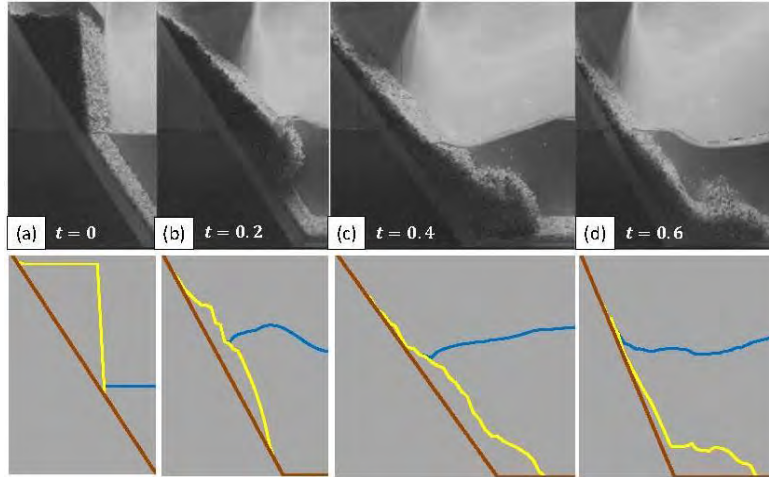

Fig 11 Landslide depth profiles at times (a) 0.0, (b) 0.2, (c) 0.4, and (d) 0.6 seconds for case 1 of benchmark #5; Visual comparison between 2LCMFlow numerical results and experimental data

2.5. Benchmark problem #7: Field case: the 1964 landslide at Port Valdez, AK

In this section, the LS3D model is applied to simulate the induced tsunamis caused by two massive SMLs, one at the head of Port Valdez (HOP) and the other at the Shoup Bay Moraine (SBM), due to the 1964 M_w 9.2 Alaska earthquake at Port Valdez, Alaska. The computational domain is discretized with considering a 50 m mesh size in both x and y directions. A 1 sec time step is also considered for the numerical simulation. Port Valdez and locations of the two SMLs are illustrated in Fig. 12 by LS3D.

Fig. 12 A three-dimensional view of Port Valdez created by LS3D including the locations of two SMLs

2.5.1. Landslide at the head of Port Valdez (HPV)

The Valdez water front was stroked with two waves as high as 6-9 *m* and with a time difference of about 10-15 *min* [19]. Fig. 13a shows the first wave at the Valdez water front predicted by LS3D. Based on this figure, the HOP landslide generates a wave with a maximum positive amplitude, a_{pmax}, of about 8.7 *m* close to the Valdez water front after 5 seconds.
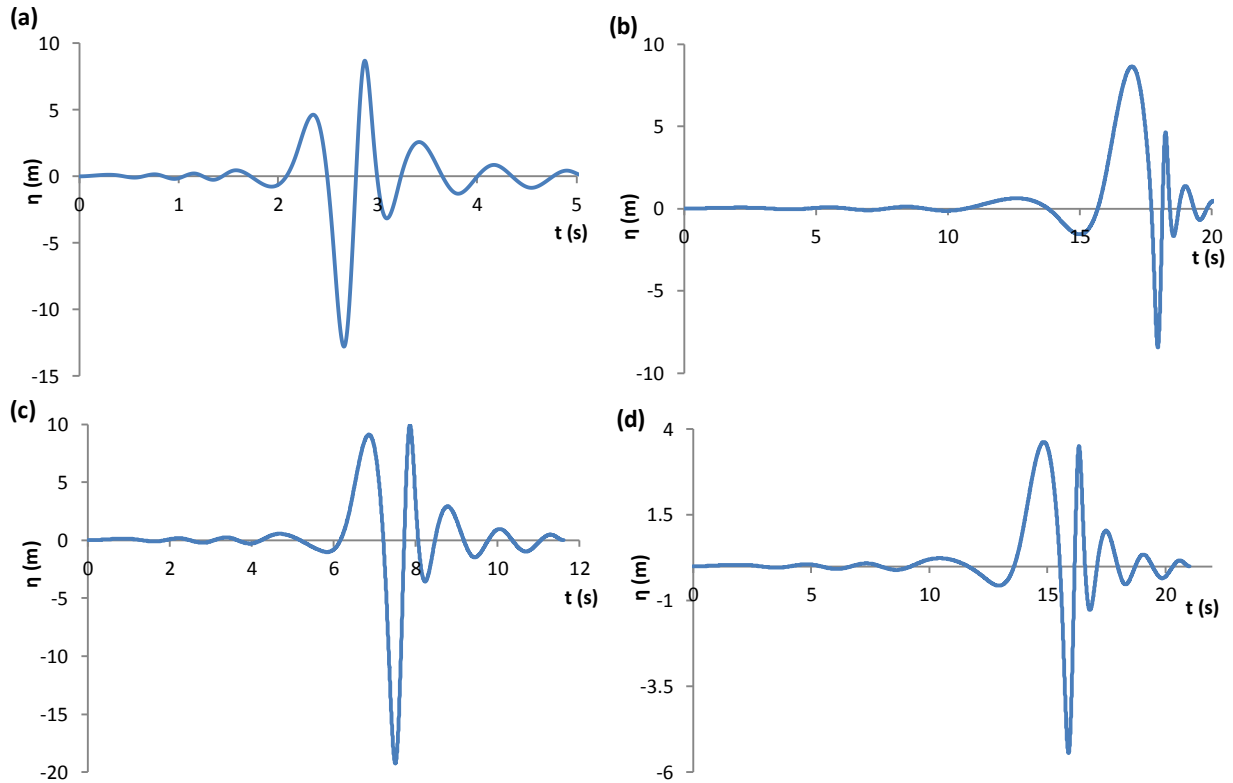

Fig. 13 Water surface fluctuations at the Valdez water front caused by (a) HPV and (b) SBM landslides, at the navigation light caused by (c) SBM landslide, and close to the Valdez Hotel caused by (d) SBM landslide.
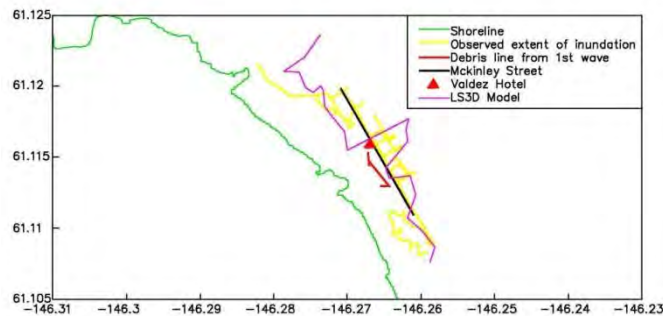

Fig. 14 Flood line due to the HPV landslide; Comparison between LS3D results and observed inundation

The inundation line estimated by LS3D for the HPV landslide is illustrated in Fig. 14 in comparison with the observed data. A simple procedure is applied to compute the maximum

distance reached by water in this region. Runup heights are calculated by Eq. 15, using the wave heights predicted by LS3D close to the related shorelines. Then, the maximum horizontal water runout distances are estimated based on the average slope of the runout path. The numerical results show that the flood not only extends through the McKinely Street but also spreads further in some areas. For a better estimation of affected areas, a more capable tool should be applied that is able to spreads the floodwater along the coast based on its natural and man-made topographical pattern.

2.5.1. Landslide at the Shoup Bay Moraine (SBM)

The second wave that reaches to the Valdez water front is initiated by the SBM landslide. This wave which is illustrated in Fig. 13b is predicted to reach to the Valdez water front in 17 seconds with maximum amplitude of about 8.6 *m*. The 10-15 *min* gap between the first and the second waves reaching to the Valdez water front is probably because of the occurrence time difference between two landslides. Based on the numerical estimations, if both landslides have been occurred at the same time, the second wave would have been reached to the shorelines about 12 seconds after the first wave. Fig 13c shows the water surface fluctuations close to the navigation light. The maximum positive wave amplitude at this point is about 9.93 *m* which is really close to the 10 *m* observed wave. The SBM landslide stimulates the water surface fluctuations shown in Fig 13d close to the Valdez Hotel. This figure indicates the arrival of a 3.62 *m* wave at this point after about 15 seconds which is much higher than the observed value of 0.5 *m*. To achieve a better estimation of this wave, the effects of water waves induced by earthquake and HPV landslides should be included in numerical simulation by applying a more capable numerical tool.

Runup heights for several points around the Port Valdez are shown in Fig. 14. As it can be observed in this figure, the runup heights vary between 18 *m* - 25 *m* along the Anderson Bay which are close enough to the observed value of about 20 *m*.

Fig. 14 Runup heights due to SBM landslide in several locations along the Port Valdez shorelines

3. Conclusions

In this report, the application of LS3D and 2LCMFlow models to the study of five benchmark problems and a real case for the 2017 NTHMP Tsunamigenic Landslide Model Benchmarking Workshop is described. Benchmarks 2 and 3 are simulated using LS3D which is a 4th order Boussinesq type model with a rigid landslide consideration. 2LCMFlow is a second-order finite volume shallow-water type model which consider landslide as a layer of a two-phase Coulomb mixture moving beneath a layer of water. Benchmarks 4 and 5 which have a deformable landslide are simulated using this model.

LGW amplitudes and runup heights are simulated with a computational error up to 10%. Although LS3D is more accurate in estimating wave propagation, the numerical dispersions cause a 10%-15% time difference between numerical and experimental LGWs. The wave characteristics close to the landslide source are estimated more accurately by 2LCMFlow. 2LCMFlow is also able to capture landslide deformations, with a computational error of less than 10%, and their effects on water surface fluctuations.

LS3D is also applied to simulate the LGWs, runup heights, and inundation caused by the 1964 landslide event of Port Valdez, Alaska. The numerical results are in a good agreement with available data. Although, considering a rigid landslide in LS3D causes an overestimation of LGW characteristics, runup heights, and flood extend in some areas. We suggest applying a numerical tool which is able to distribute the flood water along the coastal regions based on its real topographical data to achieve a better estimation of the affected areas by inundation. A GIS-based tool is a proper option in this regard.

References

1. Ataie-Ashtiani B, Najafi-Jilani A (2007) A higher-order Boussinesq-type model with moving bottom boundary: applications to submarine landslide tsunami waves. Int J Numer Methods Fluids 53(6):1019–1048. doi:10.1002/fld.1354
2. Enet F, Grilli ST, Watts P (2003) Laboratory experiments for tsunami generated by underwater landslides: Comparison with numerical modeling. Proceeding of the 30th Intl Offshore and Polar Eng Conf, Hawaii, USA, pp 372–379
3. Grilli ST, Vogelmann S, Watts P (2002) Development of a 3D numerical wave tank for modeling tsunami generation by underwater landslides. J Eng Anal Bound Elem 26:301-313. doi:10.1016/S0955-7997(01)00113-8
4. Ataie-Ashtiani B, Yavari-Ramshe S (2011) Numerical simulation of wave generated by landslide incidents in dam reservoirs. Landslides 8:417–432. doi:10.1007/s10346-011-0258-8
5. Ataie-Ashtiani B, Nik-khah A (2008) Impulsive waves caused by subaerial landslides. Environ Fluid Mech 8(3):263–280. doi:10.1007/s10652-008-9074-7
6. Yavari-Ramshe S, Ataie-Ashtiani B (2009) Simulation of wave generated by landslides in Maku dam reservoir. Prediction and Simulation Methods for Geohazard Mitigation, edited by Oka F, Kimoto S, Murakami O. Chapter 14, CRC Press. doi:10.1201/NOE0415804820.ch14

7. Lynett P, Liu PLF (2005) A numerical study of the run-up generated by three dimensional landslides. J Geophys Res 110:C03006. doi:10.1029/2004JC002443

8. Yavari-Ramshe S, Ataie-Ashtiani B (2017) A rigorous finite volume model to simulate subaerial and submarine landslide generated waves. Landslides 14(1): 203-221. doi:10.1007/s10346-015-0662-6

9. Ataie-Ashtiani B, Najafi-Jilani A (2008) Laboratory investigations on impulsive waves caused by underwater landslide. Coast Eng 55(12):989–1004. doi:10.1016/j.coastaleng.2008.03.003

10. Najafi-Jilani A, Ataie-Ashtiani B (2008) Estimation of near-field characteristics of tsunami generation by submarine landslide. Ocean Eng 35(5-6):545–557. doi:10.1016/j.oceaneng.2007.11.006

11. Yavari-Ramshe S, Ataie-Ashtiani B (2017) Subaerial landslide-generated waves: Numerical and laboratory simulations. 4th World Landslide Forum, May 29-June 3, Ljubljana, Slovenia. In: Sassa K, Mikos M, Yin Y (eds.) Advancing Culture of Living with Landslides. Springer, Cham. doi:10.1007/978-3-319-59469-9_3

12. Yavari-Ramshe S, Ataie-Ashtiani B, Sanders BF (2015) A robust finite volume model to simulate granular flows. Comput Geotech 66:96–112. doi:10.1016/j.compgeo.2015.01.015

13. Castro MJ, Ferreiro AM, García-Rodríguez JA, González-Vida JM, Macías J, Parés C, Vázquez-Cendón ME (2005) The numerical treatment of wet/dry fronts in shallow flows: application to one-layer and two-layer systems. Math Comput Model 42:419–432. doi:10.1016/j.mcm.2004.01.016

14. Synolakis CE (1987) The run-up of solitary waves. J Fluid Mech 185:523-545. doi:https://doi.org/10.1017/S002211208700329X

15. Enet F, Grilli ST (2007) Experimental study of tsunami generation by three-dimensional rigid underwater landslides. J Waterway, Port, Coastal and Ocean Eng 133(6):442-454. doi:10.1061/(ASCE)0733-950X(2007)133(6):442

16. Grilli ST, Shelby M, Kimmoun O, Dupont G, Nicolsky D, Ma G, Kirby JT, Shi F (2016) Modeling coastal tsunami hazard from submarine mass failures: effect of slide rheology, experimental validation, and case studies off the US East Coast. Nat Hazards 86(1):353-391. doi:10.1007/s11069-016-2692-3

17. Yavari-Ramshe S, Ataie-Ashtiani B (2016) Numerical simulation of subaerial and submarine landslide generated tsunami waves—recent advances and future challenges. Landslides 13(6):1325–1368. doi:10.1007/s10346-016-0734-2

18. Viroulet S, Sauret A, Kimmoun O (2014) Tsunami generated by a granular collapse down a rough inclined plane. EPL 105(34004). doi:10.1209/0295-5075/105/34004

19. Wilson BW, Tørum A (1972) Effects of the tsunamis-An engineering study, in The Great Alaska Earthquake of 1964: Washington DC, National Academy of Sciences—Engineering, p. 361–526.